IIETA International Information and Engineering Technology Association
Advancing the World of Information and Engineering

Traitement du Signal
Vol. 41, No. 4, August, 2024, pp. 1763-1779
Journal homepage: http://iieta.org/journals/ts

Spectral Similarity Based Multiscale Spatial-Spectral Preprocessing Framework for Hyperspectral Image Classification

Hasan Ali Akyürek[1*], Barış Koçer[2]

[1] Faculty of Aviation and Space Sciences, Necmettin Erbakan University, Konya 42080, Turkey
[2] Faculty of Engineering and Natural Sciences, Konya Technical University, Konya 42250, Turkey

Corresponding Author Email: hakyurek@erbakan.edu.tr

Copyright: ©2024 The authors. This article is published by IIETA and is licensed under the CC BY 4.0 license (http://creativecommons.org/licenses/by/4.0/).

https://doi.org/10.18280/ts.410410

Received: 5 April 2024
Revised: 14 June 2024
Accepted: 10 July 2024
Available online: 31 August 2024

Keywords:
Fréchet distance, hyperspectral image classification, multiscale filtering, spatial-spectral preprocessing, spectral angle mapper, spectral correlation measure, spectral information divergence, spectral similarity

ABSTRACT

Hyperspectral imaging represents an advanced technology that offers an extensive array of spectral data concerning various materials. Each pixel within a hyperspectral image encompasses reflectance or transmittance values spanning a spectrum of wavelengths, thereby constructing a spectral signature or spectral curve. Despite the high spectral resolution inherent in hyperspectral images, their spatial resolution frequently remains limited, resulting in a mixture of spectral information within the spectral signatures. This situation presents a significant obstacle to achieving precise hyperspectral image classification, given that both spectral and spatial information play pivotal roles in this endeavor. In the present investigation, a novel spectral-spatial preprocessing strategy is introduced, employing a multiscale filtering technique based on spectral similarity to enhance the accuracy of hyperspectral image classification. The methodology entails performing a neighborhood operation for each target pixel vector, predicated on their spectral resemblance. This operation assigns higher priority to more similar pixels within the neighborhood window to establish the new spectral curve of the pixel of interest. The resultant spectral curves effectively amalgamate both spatial and spectral information and are subsequently utilized during the classification process instead of the original spectral curves. The study incorporates established spectral similarity metrics alongside an innovative metric grounded in Fréchet distance to calculate spectral similarities. The outcomes derived from these metrics are juxtaposed to assess their efficacy in ameliorating the accuracy of hyperspectral image classification. Moreover, the classification performance is evaluated utilizing kernel extreme learning machine and support vector classifiers across four distinct hyperspectral image datasets. The findings underscore that, particularly when confronted with constraints related to small sample sizes, the proposed spectral-spatial preprocessing technique markedly enhances the classification accuracy of hyperspectral images.

1. INTRODUCTION

Hyperspectral imaging (HSI) is a powerful technique that captures reflection values across a broad electromagnetic spectrum for each pixel in an image. This spectral information provides valuable data for tasks such as image classification and target recognition. HSI plays a crucial role in various remote sensing applications, including environmental mapping, product analysis, and the identification and estimation of plant and mineral abundance [1].

In these applications, the primary objective is to assign specific classes to each pixel in a hyperspectral view. Traditionally, this has been achieved by treating the spectral measurements of each pixel as individual signals and applying pattern recognition techniques. For the classification of hyperspectral data, several supervised classification techniques have been developed based on techniques based solely on the spectral values of each pixel. These include Robust Sparse Representation based classification [2], Semi-supervised graph-based classification [3], Laplacian Eigen map pixel distribution flow-based classification [4], Principal Component Analysis for hyperspectral classification [5], FPCA-based kernel extreme learning machine for hyperspectral classification [6], Extended random walker-based classification [7], Genetic algorithm tuned fuzzy support vector machine for hyperspectral classification [8], Relevance Vector machines for hyperspectral classification [9].

However, in addition to spectral information, spatial content information in images is highly important for accurate classification. The use of spatial information, as well as spectral information for hyperspectral image classification, has become a primary research focus in recent years. 2DPCA-based spatial-spectral denoising [10], Discriminant sparsity preserving embedding [11], Exploiting Spectral-Spatial Information of Superpixel via Multiple Kernels [12], Attribute-profile based feature space discriminant analysis [13], Coupled compressed sensing inspired sparse spatial-spectral LSSVM [14], ensemble classification via joint sparse

representation [15], edge-preserving filtering [16], spectral-spatial adaptive total variation model [17], spatial-spectral Label Propagation [18], spatial neighborhood information and classifier combination [19].

The concept of Multiscale Spectral-Spatial Pre-processing based on neighborhood information involves leveraging information from varying neighborhood sizes in both spectral and spatial domains to enhance the processing and analysis of hyperspectral imagery. This approach aims to extract features that capture the multiscale characteristics of the data, thereby improving classification accuracy and performance.

Recently, many multiscale spatial-spectral preprocessing methods have been proposed. For example, Li et al. [20] proposed Multiscale Spatial Information Fusion, Liu et al. [21] proposed Random Multiscale Representation, Poorahangaryan and Ghassemian [22] proposed a multiscale modified minimum spanning forest, and A Hybrid Multi-scale Spatial Filtering and Minimum Spanning Forest [23] methods for spatial-spectral hyperspectral image classification. Yu et al. [24] proposed Multiscale Superpixel-Level Subspace-Based Support Vector Machines for hyperspectral image classification.

In this paper, we propose a novel multiscale spectral-spatial preprocessing algorithm that represents each pixel vector as a weighted combination of neighboring pixel vectors, taking into consideration their similarities. The rationale behind this approach is rooted in the observation that neighboring pixel vectors in a hyperspectral image exhibit similar spectral properties owing to the piecewise-continuous nature of the image. This algorithm aims to enhance the spectral-spatial characteristics of hyperspectral images by leveraging the inherent relationships between neighboring pixels. In addition to conventional spectral similarity measures, we propose the Fréchet distance as a spectral similarity measure. The focus is on the use of the Fréchet distance as a spectral similarity measure, which is a well-known metric for measuring the similarity of curves.

The subsequent sections of this paper are organized as follows: Section 2 offers a succinct summary of conventional spectral similarity metrics, the Fréchet distance, and spatial neighborhood details. Section 3 offers a brief validation of the Fréchet distance as a spectral similarity metric. Section 4 elaborates on the proposed methodology. Section 5 delineates the experimental setup and datasets. Section 6 showcases and deliberates on the experimental findings derived from four unique hyperspectral images. Finally, Section 7 encapsulates the conclusions drawn from this research endeavor.

2. RELATED WORKS

The spectral information provides important features for identifying, detecting, and classifying material. Many spectral information similarity measures, such as Spectral Angle Mapper (SAM) [25] and Spectral Information Divergence (SID) [26], which are signature vector-based similarity measures, have been proposed for this purpose, and the Spectral Correlation Measure (SCM) [27] is a spectral correlation-based similarity measure. The SAM calculates the angle between two spectra, resulting in 0 indicating high similarity and 1 indicating poor similarity. The Spectral Angle between the spectral signature and the spectral band can be calculated as Eq. (1).

$$SAM\left(s_a, s_b\right) = \cos^{-1}\left(\frac{\sum_{i=1}^{n} s_{ai} * s_{bi}}{(\sum_{i=1}^{n} s_{ai}^2)^{\frac{1}{2}} * (\sum_{i=1}^{n} s_{bi}^2)^{\frac{1}{2}}}\right) \quad (1)$$

The SID calculates the distance between p and q, and the probability distributions of spectral signatures s_a and s_b, which have n spectral bands can be calculated via Eq. (2).

$$SID(s_a, s_b) = D(s_a \parallel s_b) + D(s_b \parallel s_a) \quad (2)$$

where,

$$D(s_a \parallel s_b) = \sum_{i=1}^{n} p_i * \log(\frac{p_i}{q_i})$$

and

$$D(s_b \parallel s_a) = \sum_{i=1}^{n} q_i * \log(\frac{q_i}{p_i})$$

The SCM is calculated as the correlation coefficient between spectral signatures and spectral bands can be described by Eq. (3).

$$SCM(s_a, s_b) = \frac{n\sum_{i=1}^{n} s_{ai} * s_{bi} - \sum_{i=1}^{n} s_{ai} * \sum_{i=1}^{n} s_{bi}}{\sqrt{(n\sum_{i=1}^{n} s_{ai}^2 - (\sum_{i=1}^{n} s_{ai})^2) * (n\sum_{i=1}^{n} s_{bi}^2 - (\sum_{i=1}^{n} s_{bi})^2)}} \quad (3)$$

The Fréchet distance is a significant similarity measure used in comparing two curves, A and B, by determining the minimum leash length required for a man on one curve to walk a dog on the other curve continuously from the starting to the ending points without backtracking [28-30]. This metric captures the minimal cost of a continuous deformation of one curve into another and defines the cost of deformation as the maximal distance between two related points [31]. The Fréchet distance is a well-studied and popular measure of similarity between curves, with various studies focusing on different aspects and extensions of this concept [32].

Alt and Godau [33] studied the Fréchet distance between polygonal curves. The discrete Fréchet distance was introduced by Eiter and Mannila [29] in 1994 as an approximate solution to the Fréchet distance, specifically based on polygonal curves where only the nodes are considered. According to Li et al. [34], spectral signatures can be treated as spectral curves. This is our main idea of using the Fréchet distance as a similarity measure of spectral signatures.

However, Neighborhood operations in hyperspectral image analysis are essential for capturing both spectral and spatial information to enhance the understanding and classification of hyperspectral data. Neighborhood operations are widely used in image processing. Simply, an operator takes the values of the neighborhood around the pixel performs some operations with them, and then writes the result back on the pixel. The general procedure is described in Figure 1.

Many neighborhood operators are implemented for image processing. For example, average, count, diversity, interspersion, maximum, median, minimum, mode, quartile, range, standard deviation, sum, variance, etc. The impact of spatial resolution on neighborhood operations is crucial as it directly affects the level of detail and accuracy in spatial data analysis. Higher spatial resolution enables more precise

delineation of features within a neighborhood, facilitating better identification of patterns and relationships. However, finer spatial resolutions often result in larger datasets, leading to increased computational complexity and processing time [35]. Conversely, lower spatial resolutions may result in information loss and reduced ability to capture intricate spatial variations within neighborhoods [36].

```
For each pixel p in the hyperspectral image data
do{
    N = a neighborhood or region of the image around the pixel p
    f = a neighborhood operator function
    result(p) = f(N)
}
```

Figure 1. The general procedure of neighborhood operators

Spectral similarity measures present a method to mitigate the constraints imposed by spatial resolution in neighborhood operations. By concentrating on the spectral attributes of data rather than solely relying on spatial information, spectral similarity measures aid in identifying similarities and differences between spatial entities based on their spectral signatures. This approach allows for the comparison of spatial features at a spectral level, enabling the detection of patterns and relationships that may not be discernible from spatial data alone.

To address this limitation, we propose a similarity-based weighted neighborhood algorithm. This algorithm integrates spectral similarity measures into the neighborhood analysis, assigning weights to neighboring pixels based on their spectral similarity to the target pixel.

This similarity-based weighted neighborhood algorithm effectively enhances the analysis by emphasizing spectrally similar pixels, thereby improving the accuracy and reliability of neighborhood operations without solely depending on spatial resolution.

The influence of spatial resolution on neighborhood operations is multifaceted, impacting the level of detail, computational demands, and information loss in spatial analyses. Spectral similarity measures offer a complementary strategy to address the limitations of spatial resolution by focusing on spectral characteristics. By integrating a similarity-based weighted neighborhood algorithm, we can further enhance the analysis and interpretation of spatial data in neighborhood studies, providing a more accurate and detailed understanding of spatial patterns and relationships. For some improvement, the observations can be weighted according to their distances to the current target pixel. Therefore, nonlinear functions can be applied as weighting functions for neighborhood operators. The most classical method is the Gaussian filter. The Gaussian filter computes a weighted average of the neighborhood surrounding each pixel, with the central pixel's value exerting a greater influence on the average. The main idea of this paper is to use spectral similarities, especially the Fréchet distance, as a weighting for the weighted average neighborhood operator.

3. FRÉCHET DISTANCE AS SPECTRAL SIMILARITY METRIC

Although spectral similarity measures are effective in calculating the similarity or dissimilarity between two spectral signatures, these paired discrimination procedures alone are insufficient for distinguishing among multiple spectral classes. Furthermore, due to the differing units of measurement employed by various similarity measures, it is challenging to assess their performance without comparable statistics. To effectively discriminate among a set of spectral classes and to determine the relative performance of the aforementioned measures, three statistical algorithms were utilized: Relative Spectral Discriminatory Probability (RSDPB), Relative Spectral Discriminatory Power (RSDPW), and Relative Spectral Discriminatory Entropy (RSDE) [37, 38].

3.1 Relative spectral discriminatory probability (RSDPB)

The Relative Spectral Discriminatory Probability (RSDPB) quantifies the relative capability of all spectra within a set to be distinguished from others. Generally, a higher probability indicates a greater ability of a set of spectra to be discriminated from others. Let $\{s_k\}_{k=1}^{K}$ represent K spectral signatures in the set Δ, which serves as a database, and let t be any specific target spectral signature to be identified using Δ [37]. The RSDPB of all s_k in Δ relative to t is defined as Eq. (4).

$$P_{t,\Delta}^{m}(k) = \frac{m(t, s_k)}{\sum_{j=1}^{K} m(t, s_j)} \quad for\ k = 1, \ldots, K \tag{4}$$

where, $\sum_{j=1}^{K} m(t, s_j)$ is the normalization constant and $m(t, s_k)$ is any defined spectral similarity measure.

In our study, t can be either pure spectra or a mixture of two or more crop species, where their reflectances are combined in a linear proportion. The resulting probability vector $P_{t,\Delta}^{m} = \left(P_{t,\Delta}^{m}(1), P_{t,\Delta}^{m}(2), \ldots, P_{t,\Delta}^{m}(k)\right)^{T}$ represents the RSDPB of Δ for t, or the spectral discriminatory probability vector of Δ relative to t. Using Eq. (4), we can identify t within Δ by selecting the spectral signature with the smallest relative spectral discriminability probability. In the event of a tie, either spectral signature may be used to identify t.

RSDPB effectively normalizes the distance measure, allowing us to determine that the target matches the spectral signature with the smallest RSDPB value. Table 1 shows RSDPB values for these metrics.

Table 1. RSDPB values for the Indian pines dataset

Class Name	Fréchet	SAM	SID	SCM
CLS01	0.056	0.060	0.064	0.085
CLS02	0.079	0.087	0.065	0.007
CLS03	0.075	0.087	0.065	0.005
CLS04	0.079	0.082	0.065	0.022
CLS05	0.024	0.021	0.057	0.110
CLS06	0.050	0.042	0.062	0.102
CLS07	0.060	0.066	0.064	0.075
CLS08	0.052	0.062	0.064	0.081
CLS09	0.069	0.049	0.063	0.099
CLS10	0.076	0.089	0.065	0.013
CLS11	0.080	0.089	0.065	0.013
CLS12	0.072	0.088	0.065	0.008
CLS13	0.070	0.038	0.062	0.105
CLS14	0.024	0.011	0.047	0.111
CLS15	0.051	0.033	0.061	0.106
CLS16	0.084	0.096	0.065	0.061

3.2 Relative spectral discriminatory entropy (RSDE)

Using a selective set of spectral signatures, $\Delta = \{s_k\}_{k=1}^{K}$, we can further define the Relative Spectral Discriminatory Entropy (RSDE) measure of a spectral signature *t* for the set Δ, denoted as $H_{RSDE}(t;\Delta)$. The RSDE is given by Eq. (5).

$$H_{RSDE}(t;\Delta) = -\sum_{k=1}^{K} P_{t,\Delta}^{m}(k)\log_2\left(P_{t,\Delta}^{m}(k)\right) \quad (5)$$

Eq. (5) provides an uncertainty measure for identifying *t* using $\Delta = \{s_k\}_{k=1}^{K}$. This measure allows us to analyze the uncertainty regarding the match between *t* and the reference spectra. A larger entropy value indicates a higher degree of uncertainty concerning *t*. Conversely, the lower the entropy value, the higher the probability that the target will be correctly matched [37]. Table 2 shows RSDE values for these metrics.

Table 2. RSDE values for the Indian Pines dataset

	Fréchet	SAM	SID	SCM
RSDE	3.9300	3.8503	3.9961	3.8503

3.3 Relative spectral discriminatory power (RSDPW)

Relative Spectral Discriminatory Power (RSDPW) evaluates how effectively one spectral vector can be distinguished from another relative to a reference spectral vector [37, 38]. Given $m(.,.)$ as a spectral measure, *d* as the reference spectral signature, s_i and s_j as the spectral signatures or pair of pixel vectors, the RSDPW $m(.,.)$ is represented by Eq. (6).

$$\Omega(s_i, s_j; d) = \max\left\{\frac{m(s_i,d)}{m(s_j,d)}, \frac{m(s_j,d)}{m(s_i,d)}\right\} \quad (6)$$

Eq. (6) defines $\Omega(s_i, s_j; d)$, which provides a quantitative index of the spectral discrimination capability of a specific hyperspectral measure $m(.,.)$ between two spectral signatures and s_i and s_j relative to *d*. A higher value of $\Omega(s_i, s_j; d)$ indicates a greater discriminatory power of $m(.,.)$. Additionally, $\Omega(s_i, s_j; d)$ is symmetric and bounded below by one, i.e., $\Omega(s_i, s_j; d) \geq 1$ with equality if and only if $s_i = s_j$. RSDPW results of Fréchet Distance, SAM, SID, and SCM for the Indian pines dataset are given in Tables 3-6. respectively.

Table 3. Fréchet distance RSDPW results for the Indian pines dataset

Classes	CLS01	CLS02	CLS03	CLS04	CLS05	CLS06	CLS07	CLS08	CLS09	CLS10	CLS11	CLS12	CLS13	CLS14	CLS15	CLS16
CLS01	-	1.71	1.80	1.70	1.63	1.48	1.44	3.31	1.42	1.92	1.82	1.84	1.42	2.12	1.26	1.17
CLS02	1.71	-	9.62	4.40	2.75	1.14	1.75	1.26	1.29	6.16	5.88	6.85	1.13	3.19	1.27	1.82
CLS03	1.80	9.62	-	3.52	2.55	1.05	1.77	1.41	1.39	8.48	7.14	9.69	1.21	2.99	1.18	1.64
CLS04	1.70	4.40	3.52	-	2.71	1.17	1.50	1.24	1.26	2.59	2.54	3.06	1.11	3.15	1.25	2.14
CLS05	1.63	2.75	2.55	2.71	-	1.68	1.59	1.36	1.33	1.20	1.20	1.24	1.33	1.37	1.60	1.07
CLS06	1.48	1.14	1.05	1.17	1.68	-	1.89	1.58	3.12	1.42	1.39	1.46	2.89	1.18	3.51	1.11
CLS07	1.44	1.75	1.77	1.50	1.59	1.89	-	1.85	1.80	2.56	2.30	2.23	1.68	2.03	1.34	1.45
CLS08	3.31	1.26	1.41	1.24	1.36	1.58	1.85	-	1.54	2.10	2.05	2.10	1.52	2.09	1.28	1.26
CLS09	1.42	1.29	1.39	1.26	1.33	3.12	1.80	1.54	-	1.50	1.46	1.55	3.19	2.08	2.60	1.05
CLS10	1.92	6.16	8.48	2.59	1.20	1.42	2.56	2.10	1.50	-	8.93	7.57	1.18	3.07	1.22	1.59
CLS11	1.82	5.88	7.14	2.54	1.20	1.39	2.30	2.05	1.46	8.93	-	7.64	1.10	3.23	1.29	1.68
CLS12	1.84	6.85	9.69	3.06	1.24	1.46	2.23	2.10	1.55	7.57	7.64	-	1.28	2.86	1.12	1.72
CLS13	1.42	1.13	1.21	1.11	1.33	2.89	1.68	1.52	3.19	1.18	1.10	1.28	-	2.11	2.48	1.05
CLS14	2.12	3.19	2.99	3.15	1.37	1.18	2.03	2.09	2.08	3.07	3.23	2.86	2.11	-	1.66	1.03
CLS15	1.26	1.27	1.18	1.25	1.60	3.51	1.34	1.28	2.60	1.22	1.29	1.12	2.48	1.66	-	1.09
CLS16	1.17	1.82	1.64	2.14	1.07	1.11	1.45	1.26	1.05	1.59	1.68	1.72	1.05	1.03	1.09	-

Table 4. SAM RSDPW results for the Indian pines dataset

Classes	CLS01	CLS02	CLS03	CLS04	CLS05	CLS06	CLS07	CLS08	CLS09	CLS10	CLS11	CLS12	CLS13	CLS14	CLS15	CLS16
CLS01	-	2.66	2.61	2.87	1.87	1.72	4.24	8.68	2.30	2.53	2.51	2.59	1.30	5.08	1.03	1.99
CLS02	2.66	-	24.18	10.75	3.17	1.20	2.51	2.10	1.14	18.38	20.06	21.84	1.44	7.63	1.79	3.69
CLS03	2.61	24.18	-	10.78	3.16	1.20	2.44	2.06	1.15	18.90	22.92	33.24	1.43	7.60	1.78	3.55
CLS04	2.87	10.75	10.78	-	2.92	1.09	2.73	2.39	1.27	7.96	8.40	9.94	1.31	7.16	1.64	3.49
CLS05	1.87	3.17	3.16	2.92	-	1.98	1.44	1.48	1.71	1.28	1.28	1.29	1.97	1.66	2.46	1.23
CLS06	1.72	1.20	1.20	1.09	1.98	-	2.32	2.50	4.39	1.74	1.73	1.74	3.24	3.38	3.01	1.54
CLS07	4.24	2.51	2.44	2.73	1.44	2.32	-	6.12	2.02	3.22	3.20	3.25	1.10	5.64	1.12	2.31
CLS08	8.68	2.10	2.06	2.39	1.48	2.50	6.12	-	2.30	2.83	2.80	2.88	1.22	5.31	1.01	2.09
CLS09	2.30	1.14	1.15	1.27	1.71	4.39	2.02	2.30	-	2.03	2.02	2.05	2.36	4.04	1.76	1.71
CLS10	2.53	18.38	18.90	7.96	1.28	1.74	3.22	2.83	2.03	-	28.25	20.24	1.48	7.79	1.83	3.56
CLS11	2.51	20.06	22.92	8.40	1.28	1.73	3.20	2.80	2.02	28.25	-	22.55	1.49	7.79	1.84	3.51
CLS12	2.59	21.84	33.24	9.94	1.29	1.74	3.25	2.88	2.05	20.24	22.55	-	1.45	7.66	1.79	3.62
CLS13	1.30	1.44	1.43	1.31	1.97	3.24	1.10	1.22	2.36	1.48	1.49	1.45	-	3.02	3.22	1.48
CLS14	5.08	7.63	7.60	7.16	1.66	3.38	5.64	5.31	4.04	7.79	7.79	7.66	3.02	-	1.16	1.02
CLS15	1.03	1.79	1.78	1.64	2.46	3.01	1.12	1.01	1.76	1.83	1.84	1.79	3.22	1.16	-	1.38
CLS16	1.99	3.69	3.55	3.49	1.23	1.54	2.31	2.09	1.71	3.56	3.51	3.62	1.48	1.02	1.38	-

Table 5. SID RSDPW results for the Indian pines dataset

Classes	CLS01	CLS02	CLS03	CLS04	CLS05	CLS06	CLS07	CLS08	CLS09	CLS10	CLS11	CLS12	CLS13	CLS14	CLS15	CLS16
CLS01	-	1.06	1.07	1.06	1.09	1.03	1.46	3.17	1.05	1.07	1.06	1.08	1.02	1.36	1.03	1.03
CLS02	1.06	-	3.44	2.00	1.13	1.03	1.07	1.06	1.01	1.87	4.61	2.02	1.04	1.37	1.06	1.14
CLS03	1.07	3.44	-	1.51	1.12	1.03	1.09	1.08	1.01	3.57	5.71	5.54	1.04	1.37	1.06	1.13
CLS04	1.06	2.00	1.51	-	1.13	1.03	1.06	1.05	1.01	1.25	1.49	1.31	1.04	1.37	1.06	1.10
CLS05	1.09	1.13	1.12	1.13	-	1.21	1.02	1.03	1.10	1.01	1.01	1.01	1.10	1.23	1.25	1.01
CLS06	1.03	1.03	1.03	1.03	1.21	-	1.06	1.06	1.80	1.02	1.01	1.02	1.23	1.31	1.40	1.01
CLS07	1.46	1.07	1.09	1.06	1.02	1.06	-	2.04	1.05	1.12	1.09	1.12	1.02	1.36	1.03	1.05
CLS08	3.17	1.06	1.08	1.05	1.03	1.06	2.04	-	1.05	1.09	1.07	1.10	1.02	1.36	1.03	1.04
CLS09	1.05	1.01	1.01	1.01	1.10	1.80	1.05	1.05	-	1.02	1.02	1.02	1.15	1.33	1.15	1.02
CLS10	1.07	1.87	3.57	1.25	1.01	1.02	1.12	1.09	1.02	-	2.77	6.97	1.04	1.37	1.06	1.14
CLS11	1.06	4.61	5.71	1.49	1.01	1.01	1.09	1.07	1.02	2.77	-	2.80	1.04	1.37	1.06	1.13
CLS12	1.08	2.02	5.54	1.31	1.01	1.02	1.12	1.10	1.02	6.97	2.80	-	1.04	1.37	1.06	1.15
CLS13	1.02	1.04	1.04	1.04	1.10	1.23	1.02	1.02	1.15	1.04	1.04	1.04	-	1.29	1.75	1.01
CLS14	1.36	1.37	1.37	1.37	1.23	1.31	1.36	1.36	1.33	1.37	1.37	1.37	1.29	-	1.03	1.00
CLS15	1.03	1.06	1.06	1.06	1.25	1.40	1.03	1.03	1.15	1.06	1.06	1.06	1.75	1.03	-	1.01
CLS16	1.03	1.14	1.13	1.10	1.01	1.01	1.05	1.04	1.02	1.14	1.13	1.15	1.01	1.00	1.01	-

Table 6. SCM RSDPW results for the Indian pines dataset

Classes	CLS01	CLS02	CLS03	CLS04	CLS05	CLS06	CLS07	CLS08	CLS09	CLS10	CLS11	CLS12	CLS13	CLS14	CLS15	CLS16
CLS01	-	1.06	1.07	1.06	1.09	1.03	1.46	3.17	1.05	1.07	1.06	1.08	1.02	1.36	1.03	1.03
CLS02	1.06	-	3.44	2.00	1.13	1.03	1.07	1.06	1.01	1.87	4.61	2.02	1.04	1.37	1.06	1.14
CLS03	1.07	3.44	-	1.51	1.12	1.03	1.09	1.08	1.01	3.57	5.71	5.54	1.04	1.37	1.06	1.13
CLS04	1.06	2.00	1.51	-	1.13	1.03	1.06	1.05	1.01	1.25	1.49	1.31	1.04	1.37	1.06	1.10
CLS05	1.09	1.13	1.12	1.13	-	1.21	1.02	1.03	1.10	1.01	1.01	1.01	1.10	1.23	1.25	1.01
CLS06	1.03	1.03	1.03	1.03	1.21	-	1.06	1.06	1.80	1.02	1.01	1.02	1.23	1.31	1.40	1.01
CLS07	1.46	1.07	1.09	1.06	1.02	1.06	-	2.04	1.05	1.12	1.09	1.12	1.02	1.36	1.03	1.05
CLS08	3.17	1.06	1.08	1.05	1.03	1.06	2.04	-	1.05	1.09	1.07	1.10	1.02	1.36	1.03	1.04
CLS09	1.05	1.01	1.01	1.01	1.10	1.80	1.05	1.05	-	1.02	1.02	1.02	1.15	1.33	1.15	1.02
CLS10	1.07	1.87	3.57	1.25	1.01	1.02	1.12	1.09	1.02	-	2.77	6.97	1.04	1.37	1.06	1.14
CLS11	1.06	4.61	5.71	1.49	1.01	1.01	1.09	1.07	1.02	2.77	-	2.80	1.04	1.37	1.06	1.13
CLS12	1.08	2.02	5.54	1.31	1.01	1.02	1.12	1.10	1.02	6.97	2.80	-	1.04	1.37	1.06	1.15
CLS13	1.02	1.04	1.04	1.04	1.10	1.23	1.02	1.02	1.15	1.04	1.04	1.04	-	1.29	1.75	1.01
CLS14	1.36	1.37	1.37	1.37	1.23	1.31	1.36	1.36	1.33	1.37	1.37	1.37	1.29	-	1.03	1.00
CLS15	1.03	1.06	1.06	1.06	1.25	1.40	1.03	1.03	1.15	1.06	1.06	1.06	1.75	1.03	-	1.01
CLS16	1.03	1.14	1.13	1.10	1.01	1.01	1.05	1.04	1.02	1.14	1.13	1.15	1.01	1.00	1.01	-

Spectral similarity methods running times and comparison to fastest method are given in Table 7 and Table 8, respectively.

Table 7. Running time (second)

	Fréchet	SAM	SID	SCM
PaviaU	100.71	19.047	52.218	25.143
Salinas	56.859	15.568	38.322	21.591
KSC	106.8	28.27	63.572	38.017
Indian Pines	11.744	2.6048	7.4854	3.6197

Table 8. Running time comparison

	Fréchet	SAM	SID	SCM
PaviaU	5.3x	1.0x	2.7x	1.3x
Salinas	3.7x	1.0x	2.5x	1.4x
KSC	3.8x	1.0x	2.2x	1.3x
Indian Pines	4.5x	1.0x	2.9x	1.4x

4. MULTISCALE SPECTRAL-SPATIAL PRE-PROCESSING USING FRÉCHET DISTANCE-BASED NEIGHBORHOOD INFORMATION

In this section, we introduce a novel multiscale spectral-spatial preprocessing technique founded upon a weighted average neighborhood operator incorporating spectral similarity-based weighting. The algorithm is predicated on the premise that individual pixel vectors within a hyperspectral image exhibit spectral attributes akin to those of neighboring pixel vectors, given the prevalent continuity observed in hyperspectral imagery. For this reason, each pixel vector in a hyperspectral image will likely have similar characteristics to the weighted average of neighboring pixel vectors. To improve the characteristic similarity, the weighting function is highly important. Due to their high spectral dimensionality, spectral signatures can be represented as curves. The Fréchet distance is one of the well-known similarity measures of curves such as L-Curve, and Dynamic Time Warping (DTW). The Fréchet distance is a widely recognized curve similarity measurement method known for its effectiveness in assessing the similarity between two curves [39-41]. This metric has been extensively studied and utilized in various fields, showcasing its versatility and applicability in curve analysis. The Fréchet distance is particularly favored for its robustness and ability to accurately capture the resemblance between complex curves.

The L-curve method has gained significant popularity as a prevalent technique for choosing the regularization parameter in various applications [42, 43]. This method, known for its efficiency and reliability, utilizes curve characteristics to determine optimal parameters, contributing to enhanced model performance and accuracy.

In addition, Dynamic Time Warping (DTW) is widely adopted as a similarity measure for time series data, offering a

robust approach to aligning and comparing temporal sequences [44, 45]. DTW has proven to be instrumental in various fields, including computer science and signal processing, where precise alignment and comparison of time-dependent data are crucial.

As a result of this information, the Fréchet distance can be used as the weight of neighboring pixels in the weighted average operation. The mechanics of the weighted average operator are given in Figure 2.

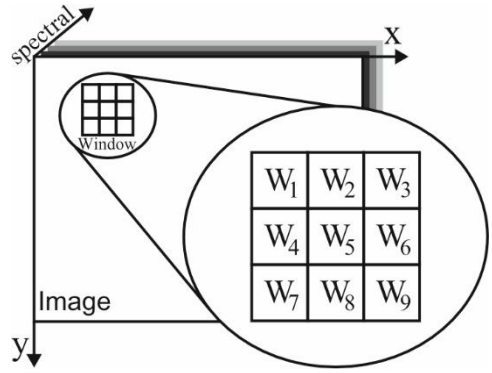

Figure 2. The mechanics of the weighted average operator

The flowchart illustrating the proposed methodology for the hyperspectral image classification can be observed in Figure 3.

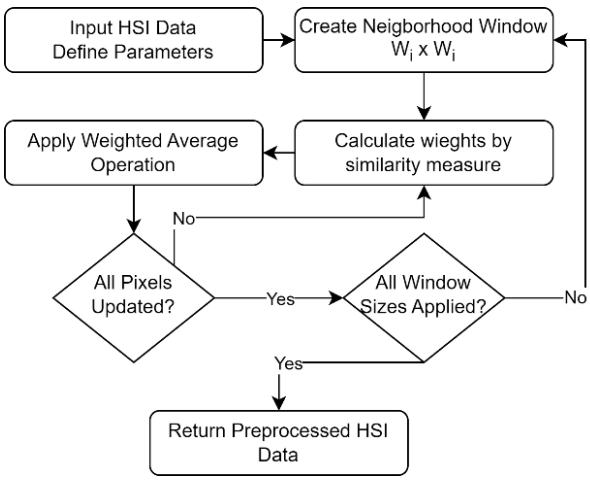

Figure 3. Flowchart of the proposed methodology

The proposed method involves the following steps:

1. Determining the Scale Size of the Window: The process begins by defining the size of the neighborhood window, which determines the spatial extent considered for analysis. This step involves selecting an appropriate scale to capture relevant spatial information effectively.

2. Selecting the Pixel Vector of the Interest-Centered Neighborhood Window: Once the window size is determined, the pixel vector of interest is selected within this neighborhood window. This pixel vector serves as the focal point for subsequent calculations.

3. Calculating Distances and Obtaining Weight Values: Distances between the pixel vector of interest and its neighboring pixel vectors are calculated using the Fréchet distance. These distances are used to derive weight values for each neighboring pixel vector, indicating their influence on the focal pixel.

4. Applying a Weighted Average Operator: A weighted average operator is then applied to calculate the new value of the pixel vector of interest. This operator considers the calculated weight values to adjust the contribution of neighboring pixels to the final value.

5. Multiscale Processing: Apply steps 2-4 iteratively for all scales.

6. Returning the Resulting Image to the Classifier: After applying steps for all scales, the resulting image, modified based on the weighted averaging process, is returned to the classifier. This modified image is used to create a classification map, enabling the classification of different regions within the hyperspectral image based on the processed pixel values.

In the first step, the neighborhood window size is defined, and the image is spatially padded. In the second step, the pixel vector of interest is selected and the neighborhood window is centrally located. In the third step, distances are calculated using the Fréchet distance, and the weight values of each neighboring pixel vector are obtained via Eq. (7).

$$w_y = 1 - f_{SS}(x, y) \tag{7}$$

where, x is the current pixel vector of interest, y is one of the neighboring pixel vectors, and f_{SS} is the spectral similarity function used to calculate the weight of pixel y, $w_y \in [0,1]$.

Finally, the weighted average operation is applied via Eq. (8).

$$g = \frac{\sum_{i=1}^{n} w_i I_i}{\sum_{i=1}^{n} w_i} \tag{8}$$

where, I is the neighborhood window which contains n pixel vectors, w_i is the weight of the ith pixel vector and g is the weighted average vector of the pixel vector of interest.

These steps are repeated by a neighborhood window for each pixel vector in the image until all scale sizes are applied. According to the above descriptions, more similar neighboring pixel vectors have greater weights because of their proximity to zero. In the realm of hyperspectral image classification, the method can be described in Figure 4.

Steps	Proposed Method
Inputs	*HSI*: MxNxD-sized Hyperspectral Image, *W*: Neighborhood window sizes vector,
Output	Classification Map
Step 1	Determine the scale size of the neighborhood window
Step 2	Create neighborhood window with size W_i, W_i
Step 3	Calculate distances and obtain weights in neighborhood windows by using the Fréchet Distance Method
Step 4	Apply a weighted average operation to update the centered pixel vector.
Step 5	Slide the window center to the next pixel vector of interest. Repeat Steps 3-5 until all pixel vectors are updated.
Step 6	Select the next window size in W and Repeat 2-6 until all window sizes applied in W
Step 7	Apply any Dimension reduction method to avoid the curse of dimensionality.
Step 7	Classify feature vectors by using any multivariate classifier. Return Classification Map

Figure 4. Pseudocodes of the proposed method

5. DATASETS AND EXPERIMENTAL DESIGN

To evaluate the effectiveness of the proposed methodology, a series of experiments were conducted using four well-known hyperspectral datasets commonly employed in hyperspectral image analysis. These datasets are recognized as standard benchmarks for assessing the performance of various classification algorithms in the field. By utilizing these datasets in the experimental validation process, a thorough evaluation of the proposed methodology's performance was ensured, allowing for its applicability across a range of hyperspectral imaging scenarios. The rigorous assessment carried out on these established datasets offers valuable insights into the method's ability to provide precise and dependable hyperspectral image classification results, thereby making a significant contribution to the advancement of research in this specialized area of study.

5.1 Indian pines dataset

The imagery capturing the Indian Pines region was obtained through the utilization of the Airborne Visible/Infrared Imaging Spectrometer (AVIRIS) sensor, which is positioned at the Indian Pines test site situated in North-Western Indiana. This imagery showcases a spatial resolution of 145×145 pixels and encompasses a spectral range of 224 bands spanning from 0.4 to 2.5 micrometers. The ground truth information delineates 16 distinct classes, as detailed in Table 9. Within the dataset, which comprises 10249 samples excluding the background, 24 spectral bands were excluded due to water absorption effects, resulting in a final count of 200 bands [46].

Table 9. Groundtruth classes and per-class samples for the Indian Pines dataset

Class Name	Class Code	Sample Count
Alfalfa	CLS01	46
Corn-no-till	CLS02	1428
Corn-min-till	CLS03	830
Corn	CLS04	237
Grass-pasture	CLS05	483
Grass-trees	CLS06	730
Grass-pasture-mowed	CLS07	28
Hay-windrowed	CLS08	478
Oats	CLS09	20
Soybean-no-till	CLS10	972
Soybean-min-till	CLS11	2455
Soybean-clean	CLS12	593
Wheat	CLS13	205
Woods	CLS14	1265
Buildings-Grass-Trees-Drives	CLS15	386
Stone-Steel-Towers	CLS16	93
	Total	**10249**

5.2 PaviaU dataset

The hyperspectral image of Pavia University was captured utilizing the ROSIS sensor in the Pavia region of northern Italy. This imagery, distinguished by a spatial resolution of 610×340 pixels, encompasses a total of 103 spectral bands spanning the wavelength range from 0.43 to 0.86μm. The ground truth data, meticulously outlined in Table 10, identifies and categorizes nine discrete classes within the dataset. This dataset, comprising 42776 samples excluding the background, is characterized by a precise geometric resolution of 1.3 meters, providing detailed spatial information for accurate analysis and classification [47].

Table 10. Groundtruth classes and per-class samples for the PaviaU dataset

Class Name	Class Code	Sample Count
Asphalt	CLS01	6631
Meadows	CLS02	18649
Gravel	CLS03	2099
Trees	CLS04	3064
Painted metal sheets	CLS05	1345
Bare Soil	CLS06	5029
Bitumen	CLS07	1330
Self-Blocking Bricks	CLS08	3682
Shadows	CLS09	947
	Total	**42776**

5.3 Salinas dataset

The captured hyperspectral image was obtained through the deployment of the Airborne Visible/Infrared Imaging Spectrometer (AVIRIS) sensor from the Salinas Valley in California. This imagery showcases a spatial resolution of 512×217 pixels and encompasses a total of 224 spectral bands spanning the range of wavelength bands from 0.4 to 2.5 micrometers. The ground truth information defines a taxonomy of 16 distinct classes, as detailed in Table 11. Within the dataset, which comprises 54129 samples excluding background noise, a subset of 20 spectral bands, known to be susceptible to water absorption effects, were meticulously eliminated. This curation process resulted in a refined dataset containing a total of 204 spectral bands, ensuring the removal of potential confounding factors and enhancing the dataset's suitability for subsequent hyperspectral image analysis [47].

Table 11. Groundtruth classes and per-class samples for the Salinas dataset

Class Name	Class Code	Sample Count
Brocoli Green Weeds_1	CLS01	2009
Brocoli Green Weeds_2	CLS02	3726
Fallow	CLS03	1976
Fallow Rough Plow	CLS04	1394
Fallow Smooth	CLS05	2678
Stubble	CLS06	3959
Celery	CLS07	3579
Grapes Untrained	CLS08	11271
Soil Vinyard Develop	CLS09	6203
Corn Senesced Green Weeds	CLS10	3278
Lettuce Romaine 4wk	CLS11	1068
Lettuce Romaine 5wk	CLS12	1927
Lettuce Romaine 6wk	CLS13	916
Lettuce Romaine 7wk	CLS14	1070
Vinyard Untrained	CLS15	7268
Vinyard Vertical Trellis	CLS16	1807
	Total	**54129**

5.4 Kennedy space center dataset

The captured hyperspectral image of the Kennedy Space Center (KSC) was captured utilizing the Airborne Visible/Infrared Imaging Spectrometer (AVIRIS) sensor at the Kennedy Space Center in Florida. This imagery, characterized by a spatial resolution of 512×614 pixels, encompasses 224 spectral bands spanning the wavelength range of 0.4-2.5μm. The ground truth information identifies 13 distinct classes, as detailed in Table 12. To mitigate issues associated with water absorption effects, 48 spectral bands were omitted from the dataset, resulting in a dataset comprising 9130 samples,

excluding the background, and a total of 176 bands [48].

Table 12. Groundtruth classes and per-class samples for the KSC dataset

Class Name	Class Code	Sample Count
Scrub	CLS01	46
Willow Swamp	CLS02	1428
Cabbage Palm Hammock	CLS03	830
Cabbage Palm/Oak Hammock	CLS04	830
Slash Pine	CLS05	237
Oak/Broadleaf Hammock	CLS06	483
Hardwood Swamp	CLS07	730
Graminoid Marsh	CLS08	28
Spartina Marsh	CLS09	478
Cattail Marsh	CLS10	20
Salt Marsh	CLS11	972
Mud Flats	CLS12	2455
Water	CLS13	593
	Total	**9130**

5.5 Experimental design

This study conducted experiments using a laptop equipped with 16 GB of Random Access Memory (RAM) and a 2700MHz i7-3740QM Central Processing Unit (CPU), with all the algorithms developed and coded in MATLAB. The proposed approach for preprocessing hyperspectral images is compared with prior research on multiscale neighborhood information. For the classification process, Support Vector Machines (SVM) [49] and Kernel Extreme Learning Machine (KELM) [50] were employed. The utilization of Support Vector Machines (SVM) was motivated by its capability to handle high-dimensional data efficiently. Recent studies have highlighted the advantages of SVM in handling problems with small sample sizes, nonlinearity, and high dimensionality, making it a popular choice in remote sensing image analysis. Moreover, the robustness of SVM, particularly attributed to the kernel function, allows for the integration of spatial characteristics into the classification process through strategies like feature fusion or composite kernels, as demonstrated in recent research.

In the conducted experiments, the spectral reflectance values were normalized to a range of [0,1] aligning with best practices in hyperspectral data preprocessing. Recent advancements in hyperspectral image classification have emphasized the importance of normalization techniques to enhance the comparability and accuracy of classification results. The determination of all parameters was carried out using the 10-fold cross-validation method, and the leave-one-out cross-validation employed for sample sizes below 10, is a widely accepted practice in model evaluation. Recent studies have shown the effectiveness of cross-validation techniques in optimizing model performance and parameter selection in remote sensing image classification.

The classification accuracies presented in this study were derived from 10 trials, ensuring robustness and reliability in the evaluation process. Recent research has emphasized the significance of comprehensive evaluation metrics in hyperspectral image classification. For instance, recent studies have utilized metrics like the kappa coefficient to compare observed accuracy with expected accuracy, providing a comprehensive assessment of classification performance. The comparison of classification accuracies based on class-wise accuracy, average accuracy, overall accuracy, standard deviation from cross-validation, and the kappa coefficient aligns with recent trends in evaluating the efficacy of classification algorithms in remote sensing applications [51].

Experimental results are compared with recently proposed methods such as MSIF [20], MOM [52], MSEPF-MMSF [22], and MSWMF-MSF [23].

6. EXPERIMENTAL RESULTS

6.1 Indian pines dataset

In the context of the Indian Pines [46] dataset, a fraction of the data, specifically 0.5%, 1%, and 5% of the samples, were randomly selected within each class to construct the learning sets, while the remaining data constituted the test set. The classification maps resulting from the application of the Support Vector Machine (SVM) classifier on the Indian Pines dataset, particularly when 5% of the samples were chosen within each class for the training set, are visually represented in Figure 5. Additionally, Table 13. provides a detailed overview of the classification accuracy for each class within the Indian Pines dataset, specifically focusing on scenarios where 5% of the samples were selected within each class for the training set, with a specific emphasis on the SVM classifier.

The experimental setup described aligns with the methodology commonly employed in hyperspectral image analysis research, where the selection of training samples from each class is crucial for evaluating the performance of classification algorithms [51]. By utilizing the SVM classifier and varying the percentage of samples chosen for training within each class, a comprehensive assessment of the classification accuracy across different classes within the Indian Pines dataset was conducted. This rigorous evaluation approach provides valuable insights into the robustness and efficacy of the proposed methodology in handling hyperspectral data with varying sample sizes and class distributions, contributing significantly to the advancement of research in hyperspectral image classification.

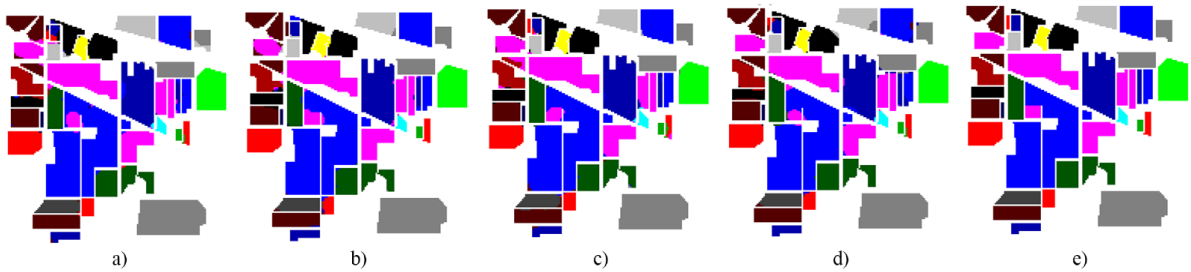

Figure 5. Classification maps obtained from the SVM classifier on the Indian Pines dataset
a) Proposed, b) SAM, c) SID, d) SCM, and e) Groundtruth

Table 13. Classwise, Average and Overall classification accuracy (%) of SVM on the Indian Pines dataset

	Fréchet			SAM			SID			SCM		
	0.5%	**1%**	**5%**	**0.5%**	**1%**	**5%**	**0.5%**	**1%**	**5%**	**0.5%**	**1%**	**5%**
CLS01	100.00	100.00	100.00	99.13	98.26	98.26	99.13	100.00	99.57	99.13	100.00	98.26
CLS02	80.94	86.05	98.00	76.67	84.66	95.57	75.88	82.40	97.38	78.54	91.61	97.65
CLS03	81.04	78.84	96.19	93.47	77.90	97.95	84.80	80.36	94.22	82.63	81.30	95.61
CLS04	99.32	93.59	98.31	96.62	98.48	95.61	97.22	95.36	97.13	97.47	96.88	96.96
CLS05	88.07	90.97	95.24	86.46	85.88	96.65	90.97	88.78	95.86	89.52	90.31	93.09
CLS06	90.36	93.78	97.81	91.64	94.85	98.68	93.42	94.49	96.16	95.64	96.47	98.82
CLS07	100.00	100.00	100.00	100.00	100.00	100.00	100.00	100.00	100.00	100.00	100.00	100.00
CLS08	92.89	96.36	99.87	99.50	97.28	99.71	99.79	98.83	99.87	98.74	98.16	100.00
CLS09	100.00	100.00	100.00	100.00	100.00	100.00	100.00	100.00	100.00	100.00	100.00	100.00
CLS10	82.37	78.95	93.66	82.02	79.47	95.68	85.89	85.45	96.15	82.37	85.10	95.39
CLS11	87.80	92.75	98.60	77.43	93.92	98.15	78.50	92.56	98.31	81.66	94.73	97.51
CLS12	86.07	83.51	95.24	84.45	86.85	94.64	84.01	87.76	96.22	84.08	88.53	96.46
CLS13	99.12	99.02	96.98	99.61	96.10	98.24	98.34	99.22	97.07	99.32	98.44	98.24
CLS14	95.97	96.17	99.46	93.47	91.86	99.59	91.46	92.05	99.91	97.23	98.01	99.81
CLS15	94.72	96.06	96.22	87.88	96.48	96.89	92.69	89.07	97.93	90.16	89.69	98.70
CLS16	98.49	98.71	97.42	97.63	98.71	98.49	97.85	98.49	98.06	100.00	99.14	94.62
Average	92.32	92.80	97.69	91.62	92.54	97.76	91.87	92.80	97.74	92.28	94.27	97.57
Overall	**88.08**	89.82	**97.48**	85.58	89.48	97.46	85.64	89.58	97.47	86.97	**92.44**	97.43
Kappa	0.86	0.88	0.97	0.84	0.88	0.97	0.84	0.88	0.97	0.85	0.91	0.97
STD	0.6252	0.8292	0.2704	0.3679	0.6254	0.1983	0.3426	0.6430	0.2265	0.6270	0.9351	0.1732

a) b) c) d) e)

Figure 6. Classification maps obtained from the KELM classifier on the Indian Pines dataset
a) Proposed, b) SAM, c) SID, d) SCM, and e) Groundtruth

Table 14. Classwise, Average and Overall classification accuracy (%) of the KELM classifier on the Indian Pines dataset

	Fréchet			SAM			SID			SCM		
	0.5%	**1%**	**5%**	**0.5%**	**1%**	**5%**	**0.5%**	**1%**	**5%**	**0.5%**	**1%**	**5%**
CLS01	100.00	100.00	99.57	99.13	99.57	98.26	99.57	100.00	99.13	100.00	100.00	99.57
CLS02	76.86	83.43	98.19	73.38	81.47	96.18	71.19	78.40	96.57	72.77	89.44	98.11
CLS03	81.42	77.81	96.05	89.90	74.53	96.75	83.81	79.93	94.31	81.98	80.65	95.01
CLS04	99.16	93.50	97.64	98.06	98.06	97.30	96.71	94.85	97.47	97.05	97.47	96.88
CLS05	86.38	90.48	94.87	86.00	85.80	95.53	89.98	88.32	94.41	88.90	89.57	92.26
CLS06	91.64	92.33	97.23	90.14	93.95	97.78	94.49	95.75	96.88	96.88	94.49	98.63
CLS07	100.00	100.00	100.00	100.00	100.00	100.00	100.00	100.00	100.00	100.00	100.00	100.00
CLS08	94.90	96.28	99.67	98.45	95.82	99.41	98.95	94.81	99.54	96.40	99.33	100.00
CLS09	100.00	100.00	100.00	100.00	100.00	100.00	100.00	100.00	100.00	100.00	100.00	100.00
CLS10	86.46	81.34	94.42	81.67	82.04	96.34	86.54	86.50	96.89	82.28	87.08	96.58
CLS11	81.90	93.15	98.73	76.79	91.10	98.48	78.26	91.82	98.31	82.57	93.43	97.83
CLS12	83.51	78.04	92.68	82.09	85.40	92.72	80.54	87.76	94.70	81.89	83.98	94.97
CLS13	99.51	99.22	97.56	99.22	96.29	98.73	98.93	99.41	98.54	99.41	98.83	98.15
CLS14	95.78	96.22	99.76	95.08	90.72	99.68	89.55	92.74	99.78	96.19	97.17	99.75
CLS15	96.32	97.62	96.79	89.95	96.32	97.41	93.37	90.93	98.29	90.88	88.03	98.13
CLS16	99.14	99.35	97.85	98.28	99.35	98.92	99.14	99.35	99.35	100.00	98.92	95.05
Average	92.06	92.42	97.56	91.13	91.90	97.72	91.31	92.54	97.76	91.70	93.65	97.56
Overall	**86.53**	89.32	97.44	84.64	87.97	97.43	84.50	88.95	97.36	86.04	**91.43**	**97.48**
Kappa	0.85	0.88	0.97	0.83	0.86	0.97	0.83	0.87	0.97	0.84	0.90	0.97
STD	0.0033	0.0022	0.0005	0.0033	0.0018	0.0008	0.0022	0.0016	0.0005	0.0020	0.0017	0.0004

Figure 6 depicts the outcomes of classification maps derived from the Kernel Extreme Learning Machine (KELM) classifier applied to the Indian Pines dataset, with a 5% sample selection in each class for the training set. The classwise classification accuracy of the KELM algorithm on the Indian Pines dataset under the same 5% sample selection in each class for the training set is presented in Table 14.

A comparison between the proposed method and other

known methods is given in Table 15. Statistical comparison of proposed method is given in Table 16.

Table 15. Comparison between the proposed method and other known methods on the Indian Pines dataset

	Proposed	MSWMF-MSF	MSEPF-MMSF	MOM	MSIF
Average	97.56	96.93	95.64	95.03	95.83
Overall	97.44	93.15	91.45	96.90	95.00
Kappa	0.97	-	0.90	0.96	0.94
STD	0.0005	-	-	-	

Table 16. Statistical comparison of proposed method

	SAM	SID	SCM
SVM	-	+	+
KELM	+	-	-

* P-Value < 0,05 denoted as +, otherwise denoted as -

6.2 PaviaU dataset

In the PaviaU [47] dataset, the entirety of the dataset is composed of samples randomly selected at rates of 0.5%, 1%, and 5% from each class to form the learning sets, with the remaining data constituting the test set. The classification maps resulting from the SVM classifier applied to the PaviaU dataset, particularly when 5% of the samples are chosen from each class for the training set, are visually depicted in Figure 7. Additionally, Table 17. provides a detailed overview of the classification accuracy of each class within the PaviaU dataset when 5% of the samples are utilized from each class for the training set, employing the SVM classifier. This meticulous experimental setup ensures a comprehensive evaluation of the proposed methodology's performance across various class distributions, shedding light on its effectiveness in handling different training set sizes and class imbalances in hyperspectral image classification scenarios.

In this section, Figure 8 illustrates the outcomes of classification maps derived from the Kernel Extreme Learning Machine (KELM) classifier applied to the PaviaU dataset, with a 5% sample selection in each class for the training set. Furthermore, Table 18 presents the classwise classification accuracy on the PaviaU dataset under the condition of 5% sample selection in each class for the training set, specifically for the KELM classifier.

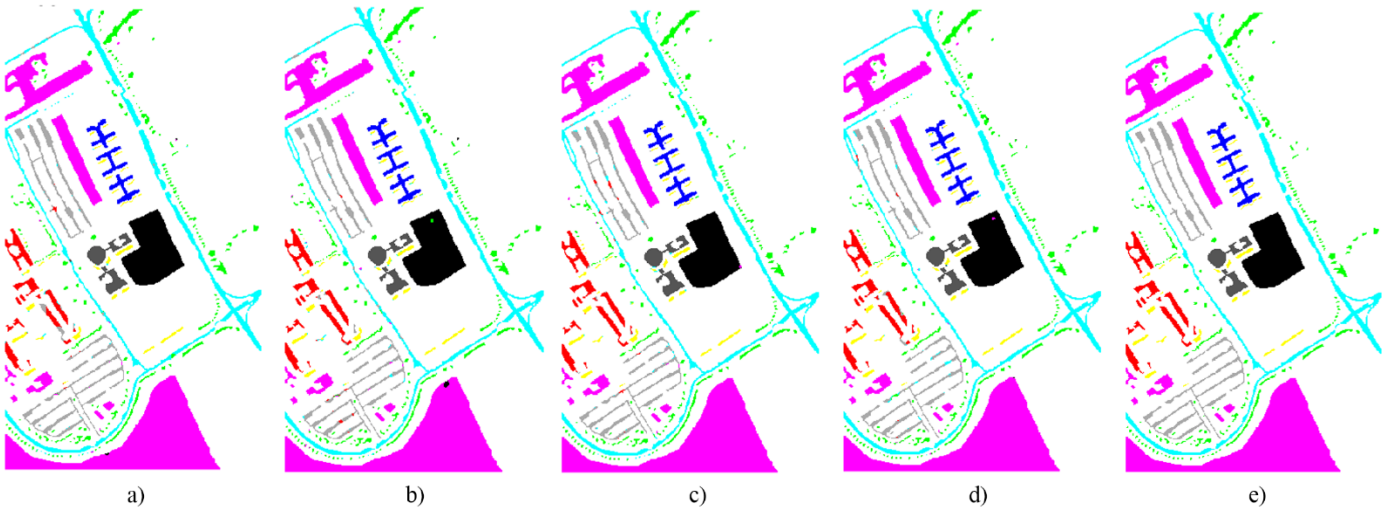

Figure 7. Classification maps generated by the SVM classifier on the PaviaU dataset
a) Proposed, b) SAM, c) SID, d) SCM, and e) Groundtruth

Table 17. Classwise, Average and Overall classification accuracy (%) of the SVM classifier on the PaviaU dataset

	Fréchet			SAM			SID			SCM		
	0.5%	**1%**	**5%**	**0.5%**	**1%**	**5%**	**0.5%**	**1%**	**5%**	**0.5%**	**1%**	**5%**
CLS01	90.27	93.00	98.71	91.07	92.92	98.56	89.23	91.26	98.62	89.09	94.01	98.68
CLS02	99.13	99.61	99.98	99.44	99.52	99.90	98.73	99.67	99.97	98.82	99.23	99.95
CLS03	77.31	85.60	94.32	75.59	86.77	95.87	76.03	88.53	97.04	78.01	81.60	94.51
CLS04	79.56	86.42	96.33	79.52	83.11	95.55	78.75	87.70	95.52	80.55	86.19	95.04
CLS05	99.69	99.58	99.91	99.66	99.41	100.00	98.96	99.63	99.93	99.03	99.85	99.97
CLS06	96.20	97.63	99.91	92.63	96.47	99.90	93.81	96.53	99.92	93.52	97.00	99.89
CLS07	98.32	98.11	99.46	98.80	98.69	100.00	97.49	97.53	99.74	98.86	98.95	99.99
CLS08	76.70	81.93	95.64	73.31	75.87	95.15	72.00	81.93	93.97	73.47	78.98	95.75
CLS09	88.32	87.88	95.29	90.71	83.63	93.92	90.86	83.80	95.21	89.29	86.84	95.21
Average	89.50	92.19	97.73	88.97	90.71	97.65	88.43	91.84	97.77	88.96	91.41	97.66
Overall	**92.76**	**94.89**	**98.74**	92.29	93.92	98.65	91.63	94.65	98.66	91.98	94.35	98.66
Kappa	0.90	0.93	0.98	0.90	0.92	0.98	0.89	0.93	0.98	0.89	0.92	0.98
STD	0.5090	0.2486	0.1627	0.4564	0.4102	0.0973	0.5167	0.3178	0.0895	0.5222	0.3888	0.1043

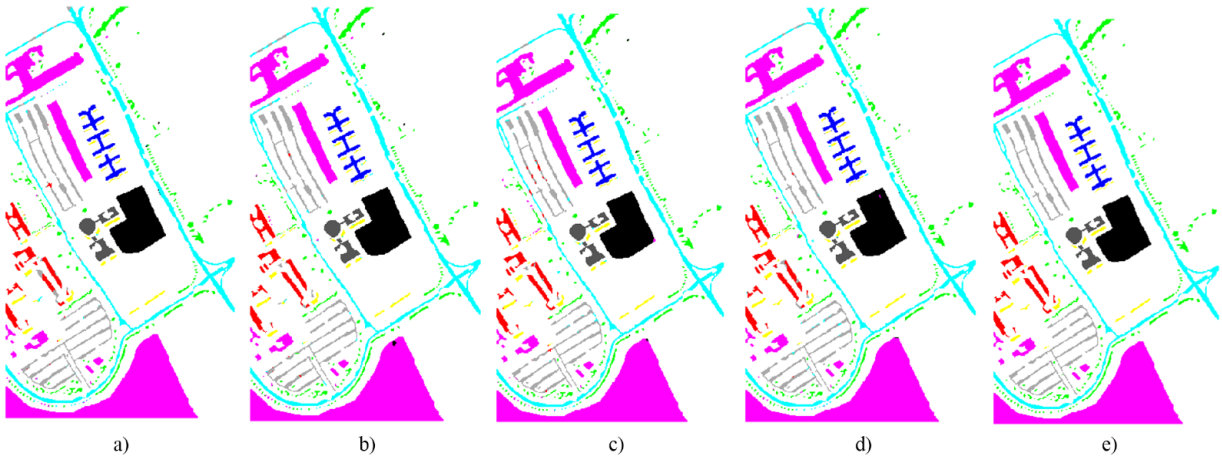

Figure 8. Classification maps obtained from the KELM classifier on the PaviaU dataset
a) Proposed, b) SAM, c) SID, d) SCM, and e) Groundtruth

Table 18. Classwise, Average and Overall classification accuracy (%) of the KELM classifier on the PaviaU dataset

	Fréchet			**SAM**			**SID**			**SCM**		
	0.5%	**1%**	**5%**	**0.5%**	**1%**	**5%**	**0.5%**	**1%**	**5%**	**0.5%**	**1%**	**5%**
CLS01	88.54	91.49	98.46	87.93	91.10	97.74	86.61	88.49	97.66	86.14	92.08	97.76
CLS02	99.40	99.78	99.99	99.24	99.62	99.92	99.03	99.75	99.96	99.21	99.68	99.98
CLS03	69.57	80.56	95.81	69.40	81.72	95.24	68.86	83.54	96.99	72.35	77.27	94.32
CLS04	64.39	77.83	93.59	64.90	72.60	92.72	60.21	77.58	92.27	63.50	71.31	90.44
CLS05	98.59	98.93	99.69	98.29	98.11	99.94	97.01	98.25	99.87	96.36	98.69	99.91
CLS06	94.77	98.43	99.96	94.50	97.49	100.00	95.28	96.46	99.81	91.68	97.64	99.92
CLS07	98.08	98.56	99.73	98.83	99.26	99.94	97.94	97.16	99.83	98.69	98.74	99.94
CLS08	66.97	78.33	97.46	63.97	73.55	97.22	67.67	77.96	95.64	66.97	70.72	96.18
CLS09	91.55	86.91	98.71	91.70	82.11	93.94	91.45	81.18	96.20	85.85	78.67	94.97
Average	85.76	90.09	98.15	85.42	88.39	97.41	84.89	88.93	97.58	84.53	87.20	97.05
Overall	**90.17**	**93.62**	**98.91**	89.76	92.54	98.48	89.44	92.82	98.43	89.25	92.11	98.22
Kappa	0.87	0.91	0.98	0.86	0.90	0.98	0.86	0.90	0.98	0.86	0.89	0.98
STD	0.0084	0.0107	0.0083	0.0068	0.0107	0.0089	0.0075	0.0092	0.0077	0.0059	0.0092	0.0077

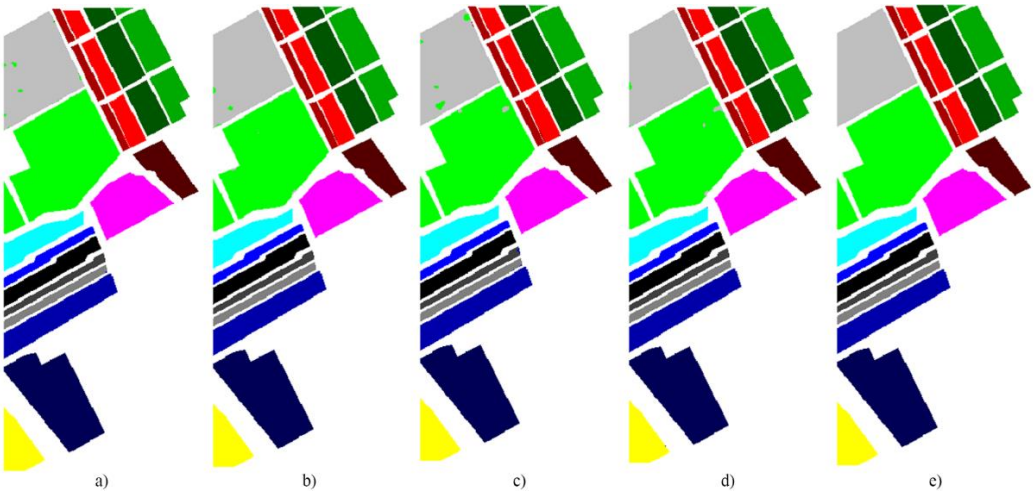

Figure 9. Classification maps obtained from the SVM classifier on the Salinas dataset
a) Proposed, b) SAM, c) SID, d) SCM, and e) Groundtruth

Table 19. Comparison between the proposed method and other known methods on the PaviaU dataset

	Proposed	**MSWMF-MSF**	**MSEPF-MMSF**	**MOM**	**MSIF**
Average	98.15	96.44	98.36	98.13	94.97
Overall	**98.91**	97.47	98.80	97.25	97.13
Kappa	0.98	-	0.98	0.96	0.96
STD	0.0083	-	-	-	

Table 20. Statistical comparison of proposed method

	SAM	**SID**	**SCM**
SVM	+	+	-
KELM	+	+	+

* P-Value < 0,05 denoted as +, otherwise denoted as –

A comparison between the proposed method and other

known methods is given in Table 19. Statistical comparison of proposed method is given in Table 20.

6.3 Salinas dataset

In the Salinas [47] dataset, a fraction of 0.5%, 1%, and 5% of the samples were randomly chosen within each class to form the training sets, while the remaining data was designated for the test set. The classification maps generated by the Support Vector Machine (SVM) classifier on the Salinas dataset, particularly when 5% of the samples were selected within each class for the training set, are visually depicted in Figure 9. Additionally, Table 21. provides a detailed overview of the classification accuracy achieved for each class in the Salinas dataset under the scenario where 5% of the samples were utilized within each class for the training set, specifically focusing on the SVM model.

Figure 10 depicts the outcomes of classification maps derived from the Kernel Extreme Learning Machine (KELM) classifier applied to the Salinas dataset, with a 5% sample selection in each class for the training set. The class-specific classification accuracy for the Salinas dataset under the same conditions is presented in Table 22 for the KELM classifier.

A comparison between the proposed method and other known methods is given in Table 23. Statistical comparison of proposed method is given in Table 24.

Table 21. Classwise, Average and Overall classification accuracy (%) of the SVM classifier on the Salinas dataset

	Fréchet			**SAM**			**SID**			**SCM**		
	0.5%	**1%**	**5%**	**0.5%**	**1%**	**5%**	**0.5%**	**1%**	**5%**	**0.5%**	**1%**	**5%**
CLS01	99.52	99.67	99.91	99.50	99.79	99.98	99.53	99.91	100.00	99.87	99.03	99.99
CLS02	99.99	100.00	100.00	100.00	100.00	100.00	100.00	100.00	100.00	100.00	100.00	100.00
CLS03	100.00	100.00	100.00	99.98	100.00	100.00	100.00	100.00	100.00	100.00	100.00	100.00
CLS04	97.98	98.65	99.56	97.86	98.42	99.28	99.08	99.27	99.57	99.05	99.57	99.40
CLS05	96.76	96.74	99.07	97.21	97.71	99.07	95.14	97.19	99.10	96.08	96.48	99.26
CLS06	99.77	99.97	100.00	100.00	99.98	99.99	99.73	99.92	100.00	99.95	99.98	99.99
CLS07	99.79	99.81	100.00	99.91	99.99	100.00	100.00	99.85	99.99	99.98	99.95	99.99
CLS08	93.90	94.93	99.63	91.52	94.88	99.47	93.39	95.05	99.53	91.14	94.81	99.54
CLS09	100.00	99.99	100.00	100.00	100.00	100.00	100.00	100.00	100.00	100.00	100.00	100.00
CLS10	97.91	99.51	99.91	98.67	99.77	99.96	98.76	99.26	99.80	98.61	99.40	99.99
CLS11	99.20	98.88	99.98	99.79	99.59	99.96	99.16	99.78	99.98	99.66	99.72	99.98
CLS12	99.76	99.99	99.99	99.72	99.93	100.00	98.80	99.97	100.00	99.75	99.93	100.00
CLS13	99.43	98.78	99.91	98.89	97.60	99.74	98.08	99.15	99.65	98.76	99.19	99.89
CLS14	98.60	94.30	99.70	98.62	94.93	99.85	95.89	98.13	99.66	92.64	97.51	99.83
CLS15	87.95	93.83	99.28	89.35	94.58	99.22	88.12	94.84	99.06	88.50	94.40	99.25
CLS16	95.43	99.36	99.86	98.30	98.30	99.93	98.33	98.57	99.45	98.04	99.21	99.59
Average	97.87	98.40	99.80	98.08	98.47	99.78	97.75	98.81	99.74	97.63	98.70	99.79
Overall	**96.51**	97.69	**99.75**	96.39	97.82	99.71	96.42	**97.95**	99.68	96.05	97.81	99.73
Kappa	0.96	0.97	1.00	0.96	0.98	1.00	0.96	0.98	1.00	0.96	0.98	1.00
STD	0.3666	0.1595	0.0482	0.3558	0.1689	0.0519	0.3934	0.2050	0.0652	0.2762	0.1779	0.0403

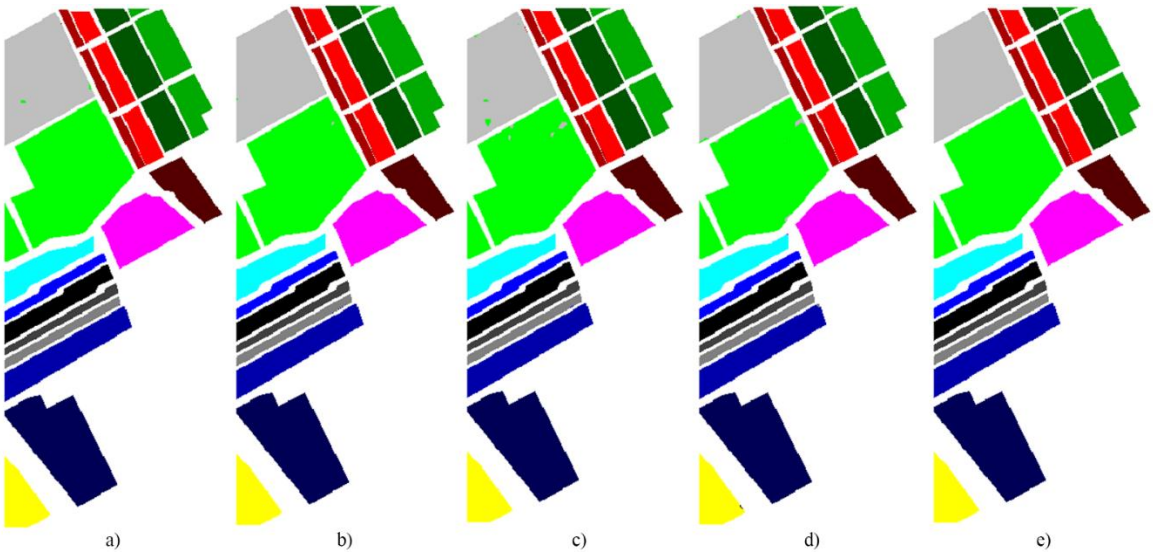

Figure 10. Classification maps obtained from the KELM classifier on the Salinas dataset
a) Proposed, b) SAM, c) SID, d) SCM, and e) Groundtruth

Table 22. Classwise, Average and Overall classification accuracy (%) of the KELM classifier on the Salinas dataset

	Fréchet			SAM			SID			SCM		
	0.5%	**1%**	**5%**	**0.5%**	**1%**	**5%**	**0.5%**	**1%**	**5%**	**0.5%**	**1%**	**5%**
CLS01	99.67	99.64	100.00	98.93	99.80	99.95	98.78	99.87	100.00	99.87	99.78	100.00
CLS02	100.00	100.00	100.00	100.00	100.00	100.00	100.00	100.00	100.00	100.00	100.00	100.00
CLS03	99.97	100.00	100.00	99.72	100.00	100.00	100.00	100.00	100.00	100.00	100.00	100.00
CLS04	99.21	99.48	99.58	98.61	99.14	99.71	99.48	99.38	99.71	99.35	99.64	99.74
CLS05	96.41	96.94	99.21	97.15	98.23	99.12	95.04	97.42	98.94	95.85	96.73	99.25
CLS06	99.22	99.75	99.97	99.76	99.83	100.00	99.36	99.59	99.97	99.74	99.73	99.98
CLS07	99.84	99.75	99.98	99.81	99.85	99.99	99.89	99.70	99.96	99.86	99.77	99.89
CLS08	95.71	96.41	99.75	93.74	96.48	99.80	94.60	96.23	99.53	94.61	95.68	99.77
CLS09	100.00	100.00	100.00	100.00	100.00	100.00	100.00	100.00	100.00	100.00	100.00	100.00
CLS10	96.11	98.75	99.75	96.60	98.71	99.78	97.45	98.82	99.59	96.88	98.85	99.90
CLS11	99.25	98.90	100.00	99.81	99.44	99.98	99.53	99.76	99.98	99.93	99.87	100.00
CLS12	99.35	99.83	100.00	98.93	99.57	99.98	99.11	99.88	100.00	99.36	99.96	99.98
CLS13	99.41	98.41	100.00	98.97	98.52	99.76	98.52	99.50	99.83	99.13	99.02	99.96
CLS14	96.24	92.34	99.53	96.67	94.79	99.81	96.43	95.83	99.68	92.17	96.49	99.83
CLS15	89.43	94.84	99.68	90.67	95.89	99.72	90.58	95.81	99.73	91.02	95.30	99.85
CLS16	96.55	99.17	99.87	98.11	98.13	99.97	98.43	98.43	99.51	97.54	99.33	99.72
Average	97.90	98.39	99.83	97.97	98.65	99.85	97.95	98.76	99.78	97.83	98.76	99.87
Overall	96.93	98.04	99.82	96.79	**98.28**	99.85	96.91	98.23	99.75	**96.95**	98.07	**99.86**
Kappa	0.97	0.98	1.00	0.96	0.98	1.00	0.97	0.98	1.00	0.97	0.98	1.00
STD	0.0020	0.0025	0.0016	0.0020	0.0028	0.0020	0.0026	0.0026	0.0017	0.0018	0.0031	0.0012

Table 23. Comparison between the proposed method and other known methods on the Salinas dataset

	Proposed	**MSWMF-MSF**	**MSEPF-MMSF**
Average	99.83	98.90	95.64
Overall	99.82	97.63	91.45
Kappa	1.00	-	0.90
STD	0.0016	-	-

Table 24. Statistical comparison of proposed method

	SAM	**SID**	**SCM**
SVM	+	-	-
KELM	+	+	+

* P-Value < 0,05 denoted as +, otherwise denoted as -

6.4 Kennedy space center dataset

In the analysis of the Kennedy Space Center (KSC) [48] dataset, a sampling approach was employed wherein data subsets of 0.5%, 1%, and 5% were randomly selected within each class for the training sets, with the remaining data comprising the test set. The outcomes of the classification maps generated by the Support Vector Machine (SVM) classifier on the Kennedy Space Center dataset, utilizing a 5% sample selection in each class for the training set, are depicted in Figure 11. Furthermore, Table 25. presents the classwise classification accuracy of the SVM on the Kennedy Space Center dataset under the condition of 5% sample selection in each class for the training set.

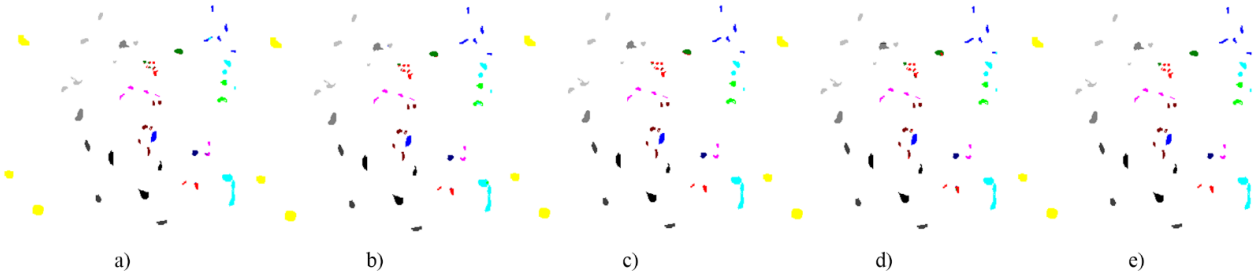

Figure 11. Classification maps obtained from the SVM classifier on the Kennedy Space Center dataset
a) Proposed, b) SAM, c) SID, d) SCM, and e) Groundtruth

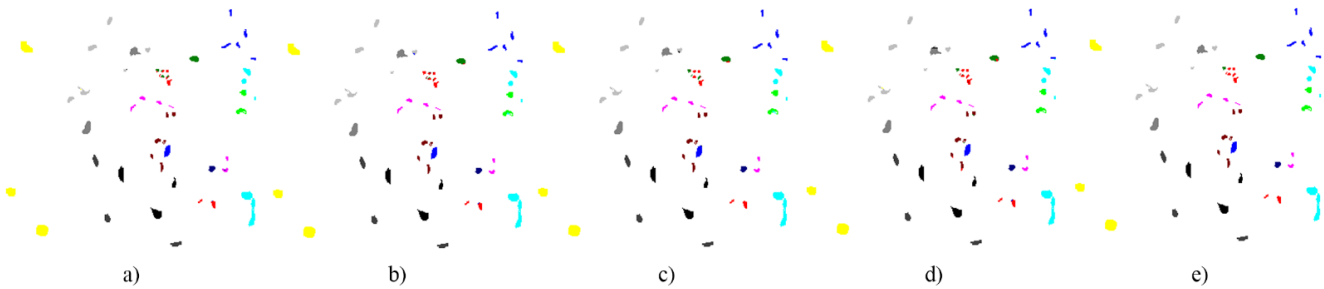

Figure 12. Classification maps obtained from the KELM classifier on the Kennedy Space Center dataset
a) Proposed, b) SAM, c) SID, d) SCM, and e) Groundtruth

Table 25. Classwise, Average and Overall classification accuracy (%) of the SVM classifier on the KSC dataset

	Fréchet			SAM			SID			SCM		
	0.5%	**1%**	**5%**	**0.5%**	**1%**	**5%**	**0.5%**	**1%**	**5%**	**0.5%**	**1%**	**5%**
CLS01	98.58	97.98	100.00	99.08	95.16	99.03	96.53	96.79	99.82	99.84	98.27	100.00
CLS02	96.71	94.40	98.19	98.19	97.04	99.75	96.71	99.59	97.04	98.35	90.53	98.52
CLS03	94.84	95.39	98.59	94.14	98.20	97.34	95.94	98.52	97.34	94.22	93.05	97.81
CLS04	84.44	82.94	89.29	82.30	78.57	92.14	82.38	78.97	83.81	73.17	80.71	83.25
CLS05	89.69	90.93	88.82	95.28	94.78	92.92	87.83	90.43	84.35	96.15	95.16	93.79
CLS06	96.94	97.29	95.90	97.64	99.04	97.21	96.51	93.97	98.08	96.94	96.42	97.03
CLS07	99.81	100.00	99.62	99.43	100.00	100.00	100.00	100.00	100.00	99.62	100.00	98.86
CLS08	98.79	98.52	97.82	97.22	97.45	100.00	95.27	96.52	98.65	96.15	98.10	97.40
CLS09	87.65	100.00	100.00	96.96	100.00	100.00	97.54	97.23	100.00	97.88	100.00	100.00
CLS10	99.11	99.46	99.70	100.00	99.75	100.00	99.90	100.00	100.00	99.95	100.00	99.16
CLS11	97.95	99.57	99.76	96.28	97.80	98.09	98.14	98.66	99.71	98.57	98.47	99.57
CLS12	95.71	97.46	99.56	95.75	96.66	99.92	95.47	97.26	99.96	96.50	98.53	99.56
CLS13	99.98	100.00	100.00	99.94	100.00	100.00	100.00	100.00	100.00	100.00	100.00	100.00
Average	95.40	96.46	97.48	96.32	96.50	98.19	95.55	96.00	96.83	95.95	96.10	97.30
Overall	96.19	**97.55**	98.53	97.12	97.10	**98.83**	96.53	96.93	98.22	**97.07**	97.30	98.31
Kappa	0.96	0.97	0.98	0.97	0.97	0.99	0.96	0.97	0.98	0.97	0.97	0.98
STD	0.3477	0.5309	0.2597	0.2839	0.4176	0.2054	0.3081	0.6338	0.2338	0.4463	0.3609	0.2636

Table 26. Classwise, Average and Overall classification accuracy (%) of the KELM classifier on the KSC dataset

	Fréchet			SAM			SID			SCM		
	0.5%	**1%**	**5%**	**0.5%**	**1%**	**5%**	**0.5%**	**1%**	**5%**	**0.5%**	**1%**	**5%**
CLS01	98.82	99.50	100.00	99.32	97.29	99.79	96.53	98.58	100.00	100.00	99.82	100.00
CLS02	97.70	94.40	99.26	98.68	96.71	99.75	96.71	99.92	97.86	98.85	90.86	98.52
CLS03	94.77	95.86	99.45	94.92	97.50	97.73	96.48	96.02	98.44	97.27	94.84	97.34
CLS04	82.46	86.19	91.43	82.54	79.05	91.91	82.14	82.38	85.00	74.05	85.16	80.79
CLS05	93.66	96.40	95.53	97.02	98.39	93.04	95.28	94.29	94.66	98.51	97.52	97.64
CLS06	98.08	99.30	95.02	99.21	99.56	99.04	98.08	97.12	96.94	98.43	96.59	98.43
CLS07	100.00	100.00	99.81	99.81	100.00	100.00	100.00	100.00	100.00	100.00	100.00	99.81
CLS08	99.81	98.28	99.77	99.49	98.70	100.00	95.87	97.22	98.89	95.73	98.05	98.38
CLS09	87.08	100.00	100.00	96.96	100.00	100.00	96.88	97.23	100.00	97.92	100.00	100.00
CLS10	99.36	99.65	100.00	100.00	99.75	100.00	100.00	100.00	100.00	100.00	100.00	100.00
CLS11	98.33	99.43	99.67	96.85	97.80	98.66	98.38	98.62	99.47	98.71	98.76	99.57
CLS12	97.30	96.30	98.93	97.53	97.50	99.44	97.22	98.45	99.64	96.62	98.93	99.48
CLS13	100.00	100.00	100.00	100.00	100.00	100.00	100.00	100.00	100.00	100.00	100.00	100.00
Average	95.95	97.33	98.37	97.10	97.10	98.41	96.43	96.91	97.76	96.62	96.96	97.69
Overall	96.58	**98.08**	99.01	**97.78**	97.70	**99.04**	97.02	97.67	98.63	97.45	97.99	98.51
Kappa	0.96	0.98	0.99	0.98	0.97	0.99	0.97	0.97	0.98	0.97	0.98	0.98
STD	0.0055	0.0072	0.0094	0.0079	0.0061	0.0090	0.0060	0.0068	0.0123	0.0081	0.0092	0.0093

Table 27. Statistical comparison of proposed method

	SAM	**SID**	**SCM**
SVM	+	-	-
KELM	-	-	-

*P-Value < 0,05 denoted as +, otherwise denoted as -

In Figure 12, the outcomes of classification maps derived from the Kernel Extreme Learning Machine (KELM) classifier on the Kennedy Space Center dataset are depicted, wherein a 5% sample is chosen from each class for the training set. The classwise classification accuracy of the KELM algorithm on the Kennedy Space Center dataset, with 5% of the samples selected from each class in the training set, is presented in Table 26. Statistical comparison of proposed method is given in Table 27.

7. CONCLUSION

In this study, a novel spectral-spatial preprocessing technique is introduced, leveraging a weighted average neighborhood operator with spectral similarity-based weighting to enhance the classification precision of hyperspectral images. Recent research has highlighted the significance of spatial preprocessing algorithms in hyperspectral image analysis. For instance, a spatial preprocessing (SPP) algorithm has been proposed, estimating spatially-derived factors for each pixel vector to weigh the spectral information based on its spatial context. This emphasizes the growing interest in incorporating spatial information to refine hyperspectral image processing methods.

The fundamental concept underlying the algorithm is rooted in the notion that each pixel vector within a hyperspectral image shares spectral attributes akin to those of its neighboring pixel vectors, given the prevalent continuity typically observed in hyperspectral imagery. Recent studies have shown the advantage of integrating spatial information with spectral data to enhance the representation of image properties in a lower-dimensional space. This underscores the importance of considering spatial correlations in hyperspectral imagery for more accurate analysis and classification.

Moreover, the efficacy of the proposed approach heavily relies on the weighting function employed to enhance the similarity of characteristics. Spatial postprocessing techniques have been investigated to create more homogeneous thematic maps, emphasizing the role of spatial information in refining hyperspectral image analysis. By incorporating spatial information into the preprocessing stage, recent advancements have demonstrated improved feature extraction and classification accuracy in hyperspectral imagery.

Given the elevated spectral dimensionality inherent in hyperspectral data, spectral signatures are often represented as curves. The Fréchet distance emerges as a well-established metric for measuring the similarity between curves. Recent studies have utilized the Fréchet distance as a weighting factor for neighboring pixels within the weighted average operation, showcasing its effectiveness in enhancing hyperspectral image classification outcomes. This highlights the growing trend of leveraging advanced similarity measures to optimize spectral-spatial preprocessing techniques for hyperspectral image analysis. To evaluate the performance of the proposed method, a comparative analysis is conducted against three prevalent spectral similarity measures: Spectral Angle Mapper (SAM) [53], Spectral Information Divergence (SID) [26], and Spectral Correlation Measure (SCM) [27].

In the classification phase, Support Vector Machines (SVM) [49] and Kernel Extreme Learning Machine (KELM) [50] are employed as classification algorithms. The classification outcomes obtained through the proposed method are juxtaposed with those derived from recently introduced methodologies such as MSIF [20], MOM [52], MSEPF-MMSF [22], and MSWMF-MSF [23]. The experimental findings underscore a substantial enhancement in classification accuracy facilitated by the proposed method. Notably, the utilization of the Fréchet distance as a weighting mechanism for neighboring pixels outperforms the conventional spectral similarity measures, signifying its efficacy in refining the classification outcomes of hyperspectral images.

REFERENCES

[1] Landgrebe, D. (2002). Hyperspectral image data analysis. IEEE Signal Processing Magazine, 19(1): 17-28. https://doi.org/10.1109/79.974718

[2] Li, C., Ma, Y., Mei, X., Liu, C., Ma, J. (2016). Hyperspectral image classification with robust sparse representation. IEEE Geoscience and Remote Sensing Letters, 13(5): 641-645. https://doi.org/10.1109/lgrs.2016.2532380

[3] Camps-Valls, G., Marsheva, T.V.B., and Zhou, D. (2007). Semi-supervised graph-based hyperspectral image classification. IEEE Transactions on Geoscience and Remote Sensing, 45(10): 3044-3054. https://doi.org/10.1109/TGRS.2007.895416

[4] Hou, B., Zhang, X., Ye, Q., Zheng, Y. (2013). A novel method for hyperspectral image classification based on Laplacian eigenmap pixels distribution-flow. IEEE Journal of Selected Topics in Applied Earth Observations and Remote Sensing, 6(3): 1602-1618. https://doi.org/10.1109/jstars.2013.2259470

[5] Rodarmel, C., Shan, J. (2002). Principal component analysis for hyperspectral image classification. Surveying and Land Information Science, 62(2): 115.

[6] Wei, Y., Xiao, G., Deng, H., Chen, H., Tong, M., Zhao, G., Liu, Q. (2015). Hyperspectral image classification using FPCA-based kernel extreme learning machine. Optik - International Journal for Light and Electron Optics, 126(23): 3942-3948. https://doi.org/10.1016/j.ijleo.2015.07.184

[7] Kang, X., Li, S., Fang, L., Li, M., Benediktsson, J.A. (2015). Extended random walker-based classification of hyperspectral images. IEEE Transactions on Geoscience and Remote Sensing, 53(1): 144-153. https://doi.org/10.1109/tgrs.2014.2319373

[8] Zhou, M. (2012). Classification of urban vegetation patterns from hyperspectral imagery: Hybrid algorithm based on genetic algorithm tuned fuzzy support vector machine. Optical Engineering, 51(11): 111709. https://doi.org/10.1117/1.oe.51.11.111709

[9] Demir, B., Erturk, S. (2007). Hyperspectral image classification using relevance vector machines. IEEE Geoscience and Remote Sensing Letters, 4(4): 586-590. https://doi.org/10.1109/lgrs.2007.903069

[10] Huang, J., Ma, Y., Mei, X., Fan, F. (2016). A hybrid spatial-spectral denoising method for infrared hyperspectral images using 2DPCA. Infrared Physics & Technology, 79: 68-73. https://doi.org/10.1016/j.infrared.2016.09.009

[11] Han, M., Zhang, C. (2017). Spectral-spatial classification of hyperspectral image based on discriminant sparsity preserving embedding. Neurocomputing, 243: 133-141. https://doi.org/10.1016/j.neucom.2017.03.009

[12] Fang, L., Li, S., Duan, W., Ren, J., Benediktsson, J.A. (2015). Classification of hyperspectral images by exploiting spectral–spatial information of Superpixel via multiple kernels. IEEE Transactions on Geoscience and Remote Sensing, 53(12): 6663-6674. https://doi.org/10.1109/tgrs.2015.2445767

[13] Imani, M., Ghassemian, H. (2017). Attribute profile based feature space discriminant analysis for spectral-spatial classification of hyperspectral images. Computers & Electrical Engineering, 62: 555-569. https://doi.org/10.1016/j.compeleceng.2016.09.029

[14] Yang, L., Yang, S., Li, S., Zhang, R., Liu, F., Jiao, L. (2015). Coupled compressed sensing inspired sparse spatial-spectral LSSVM for hyperspectral image classification. Knowledge-Based Systems, 79: 80-89. https://doi.org/10.1016/j.knosys.2015.01.006

[15] Zhang, E., Zhang, X., Jiao, L., Li, L., Hou, B. (2016). Spectral–spatial hyperspectral image ensemble classification via joint sparse representation. Pattern Recognition, 59: 42-54. https://doi.org/10.1016/j.patcog.2016.01.033

[16] Kang, X., Li, S., Benediktsson, J.A. (2014). Spectral–spatial hyperspectral image classification with edge-preserving filtering. IEEE Transactions on Geoscience and Remote Sensing, 52(5): 2666-2677. https://doi.org/10.1109/TGRS.2013.2264508

[17] Yuan, Q., Zhang, L., Shen, H. (2021). Hyperspectral image denoising employing a spectral–spatial adaptive total variation model. IEEE Transactions on Geoscience and Remote Sensing, 50(10): 3660-3677. https://doi.org/10.1109/TGRS.2012.2185054

[18] Wang, L., Hao, S., Wang, Q., Wang, Y. (2014). Semi-supervised classification for hyperspectral imagery based on spatial-spectral Label Propagation. ISPRS Journal of Photogrammetry and Remote Sensing, 97: 123-137.

https://doi.org/10.1016/j.isprsjprs.2014.08.016
[19] Tan, K., Hu, J., Li, J., and Du, P. (2015). A novel semi-supervised hyperspectral image classification approach based on spatial neighborhood information and classifier combination. ISPRS Journal of Photogrammetry and Remote Sensing, 105: 19-29. https://doi.org/10.1016/j.isprsjprs.2015.03.006
[20] Li, H., Song, Y., Chen, C.L.P. (2017). Hyperspectral image classification based on multiscale spatial information fusion. IEEE Transactions on Geoscience and Remote Sensing, 55(9): 5302-5312. https://doi.org/10.1109/TGRS.2017.2705176
[21] Liu, J., Wu, Z., Li, J., Xiao, L., Plaza, A., Benediktsson, J.A. (2016). Spatial–spectral hyperspectral image classification using random multiscale representation. IEEE Journal of Selected Topics in Applied Earth Observations and Remote Sensing, 9(9): 4129-4141. https://doi.org/10.1109/jstars.2016.2587678
[22] Poorahangaryan, F., Ghassemian, H. (2017). A multiscale modified minimum spanning forest method for spatial-spectral hyperspectral images classification. EURASIP Journal on Image and Video Processing, 2017(1): 71. https://doi.org/10.1186/s13640-017-0219-9
[23] Poorahangaryan, F., Ghassemian, H. (2017). A hybrid multi-scale spatial filtering and minimum spanning forest for spectral–spatial hyperspectral image classification. Journal of the Indian Society of Remote Sensing, 46: 345-353. https://doi.org/10.1007/s12524-017-0669-7
[24] Yu, H., Gao, L., Liao, W., Zhang, B., Pizurica, A., Philips, W. (2017). Multiscale superpixel-level subspace-based support vector machines for hyperspectral image classification. IEEE Geoscience and Remote Sensing Letters, 14(11): 2142-2146. https://doi.org/10.1109/lgrs.2017.2755061
[25] Kruse, F.A., Lefkoff, A.B., Boardman, J.W., Heidebrecht, K.B., Shapiro, A.T., Barloon, P.J., Goetz, A.F.H. (1993). The spectral image processing system (SIPS)—interactive visualization and analysis of imaging spectrometer data. Remote Sensing of Environment, 44(2-3): 145-163. https://doi.org/10.1016/0034-4257(93)90013-n
[26] Chein, I.C. (2000). An information-theoretic approach to spectral variability, similarity, and discrimination for hyperspectral image analysis. IEEE Transactions on Information Theory, 46(5): 1927-1932. https://doi.org/10.1109/18.857802
[27] van der Meero, F., Bakker, W. (1997). Cross correlogram spectral matching: Application to surface mineralogical mapping by using AVIRIS data from Cuprite, Nevada. Remote Sensing of Environment, 61(3): 371-382. https://doi.org/10.1016/s0034-4257(97)00047-3
[28] Fan, C., Raichel, B. (2020). Computing the fréchet gap distance. Discrete & Computational Geometry, 65(4): 1244-1274. https://doi.org/10.1007/s00454-020-00224-w
[29] Eiter, T., Mannila, H. (1994). Computing discrete Fréchet distance. Citeseer.
[30] Fréchet, M.M. (1906). Sur quelques points du calcul fonctionnel. Rendiconti del Circolo Matematico di Palermo, 22(1): 1-72. https://doi.org/10.1007/bf03018603
[31] Maheshwari, A., Sack, J.R., Scheffer, C. (2018). Approximating the integral fréchet distance. Computational Geometry, 70-71: 13-30. https://doi.org/10.1016/j.comgeo.2018.01.001
[32] Bringmann, K., Künnemann, M. (2017). Improved approximation for Fréchet distance on C-packed curves matching conditional lower bounds. International Journal of Computational Geometry & Applications, 27(01n02): 85-119. https://doi.org/10.1142/s0218195917600056
[33] Alt, H., Godau, M. (1995). Computing the FrÉchet distance between two polygonal curves. International Journal of Computational Geometry & Applications, 05(01n02): 75-91. https://doi.org/10.1142/s0218195995000064
[34] Li, H., Xiao, G., Xia, T., Tang, Y.Y., Li, L. (2014). Hyperspectral image classification using functional data analysis. IEEE Transactions on Cybernetics, 44(9): 1544-1555. https://doi.org/10.1109/TCYB.2013.2289331
[35] Maynard, J.J., Johnson, M.G. (2014). Scale-dependency of LiDAR derived terrain attributes in quantitative soil-landscape modeling: Effects of grid resolution vs. neighborhood extent. Geoderma, 230-231: 29-40. https://doi.org/10.1016/j.geoderma.2014.03.021
[36] Wu, Z., Chen, L. (2017). Optimizing the spatial arrangement of trees in residential neighborhoods for better cooling effects: Integrating modeling with in-situ measurements. Landscape and Urban Planning, 167: 463-472. https://doi.org/10.1016/j.landurbplan.2017.07.015
[37] Chang, C.I. (2000). An information-theoretic approach to spectral variability, similarity, and discrimination for hyperspectral image analysis. IEEE Transactions on Information Theory, 46(5): 1927-1932. https://doi.org/10.1109/18.857802
[38] Van der Meer, F. (2006). The effectiveness of spectral similarity measures for the analysis of hyperspectral imagery. International Journal of Applied Earth Observation and Geoinformation, 8(1): 3-17. https://doi.org/10.1016/j.jag.2005.06.001
[39] Bringmann, K. (2014). Why walking the dog takes time: Frechet distance has no strongly Subquadratic algorithms unless SETH fails. In 2014 IEEE 55th Annual Symposium on Foundations of Computer Science (FOCS), pp. 661-670.
[40] Toohey, K., Duckham, M. (2015). Trajectory similarity measures. SIGSPATIAL Special, 7(1): 43-50. https://doi.org/10.1145/2782759.2782767
[41] Gudmundsson, J., van Renssen, A., Saeidi, Z., Wong, S. (2021). Translation invariant Fréchet distance queries. Algorithmica, 83: 3514-3533. https://doi.org/10.1007/s00453-021-00865-0
[42] Hansen, P.C., O'Leary, D.P. (1993). The use of the L-curve in the regularization of discrete Ill-posed problems. SIAM Journal on Scientific Computing, 14(6): 1487-1503. https://doi.org/10.1137/0914086
[43] Xu, Y., Pei, Y., Dong, F. (2016). An extended L-curve method for choosing a regularization parameter in electrical resistance tomography. Measurement Science and Technology, 27(11): 114002. https://doi.org/10.1088/0957-0233/27/11/114002
[44] Teeraratkul, T., O'Neill, D., Lall, S. (2018). Shape-based approach to household electric load curve clustering and prediction. IEEE Transactions on Smart Grid, 9(5): 5196-5206. https://doi.org/10.1109/TSG.2017.2683461
[45] Buchin, K., Nusser, A., Wong, S. (2022). Computing

continuous dynamic time warping of time series in polynomial time. arXiv preprint arXiv:2203.04531.
[46] Baumgardner, M.F., Biehl, L.L., Landgrebe, D.A. (2015). 220 band AVIRIS hyperspectral image data set: June 12, 1992 Indian pine test site 3. Purdue University Research Repository. https://doi.org/10.4231/R7RX991C
[47] AVIRIS Salinas Valley and ROSIS Pavia University Hyperspectral Datasets. http://www.ehu.es/ccwintco/index.php/Hyperspectral_Remote_Sensing_Scenes.
[48] AVIRIS Kennedy Space Center Hyperspectral Dataset. http://www.ehu.es/ccwintco/index.php/Hyperspectral_Remote_Sensing_Scenes.
[49] Chang, C.C., Lin, C.J. (2011). LIBSVM: A library for support vector machines. ACM Transactions on Intelligent Systems and Technology (TIST), 2(3): 27.
[50] Pal, M., Maxwell, A.E., Warner, T.A. (2013). Kernel-based extreme learning machine for remote-sensing image classification. Remote Sensing Letters, 4(9): 853-862. https://doi.org/10.1080/2150704x.2013.805279
[51] Cohen, J. (1960). A coefficient of agreement for nominal scales. Educational and Psychological Measurement, 20(1): 37-46. https://doi.org/10.1177/001316446002000104
[52] Liu, J., Wu, Z., Li, J., Xiao, L., Plaza, A., Benediktsson, J.A. (2016). Spatial-spectral hyperspectral image classification using random multiscale representation. IEEE Journal of Selected Topics in Applied Earth Observations and Remote Sensing, 9(9): 4129-4141. https://doi.org/10.1109/JSTARS.2016.2587678
[53] Kruse, F.A., Lefkoff, A.B., Boardman, J.W., Heidebrecht, K.B., Shapiro, A.T., Barloon, P.J., Goetz, A.F.H. (1993). The spectral image processing system (SIPS)—interactive visualization and analysis of imaging spectrometer data. Remote Sensing of Environment, 44(2): 145-163. https://doi.org/10.1016/0034-4257(93)90013-N